ACS Photonics

pubs.acs.org/journal/apchd5

Article

Multiplexed Chromatin Analysis Using Optical Spectroscopic Statistical Nanosensing

Yuanzhe Su, Luay M. Almassalha, Nicolas Acosta, Cody L. Dunton, Karla I. Medina, Emily Pujadas Liwag, Geng Wang,* and Vadim Backman*

Cite This: https://doi.org/10.1021/acsphotonics.5c00311

Read Online

ACCESS | Metrics & More | Article Recommendations | Supporting Information

ABSTRACT: In single cells, chromatin packs into organized structures to perform biological functions, such as RNA transcription regulation. Characterizing such structural behaviors, including packing density and mass scaling, is critical in epigenetics research. Partial wave spectroscopic (PWS) microscopy is a label-free, live-cell, high-throughput imaging modality that utilizes optical spectroscopic statistical nanosensing. Rather than resolving the exact chromatin packing structure, PWS extracts statistical packing information from spectroscopic interference signals. In this study, we evaluate its ability to characterize multiplexed chromatin packing density and mass scaling, as well as its spatial confidence interval, using finite difference time domain (FDTD) electromagnetic simulations. We validated the simulation-based analysis algorithm by comparing experimental PWS images against coregistered super-resolution acquisitions, confirming its accuracy in capturing chromatin packing metrics. We then applied this modality to live cells treated with different epigenetic agents, mapping spatial changes in chromatin packing in a high-throughput workflow.

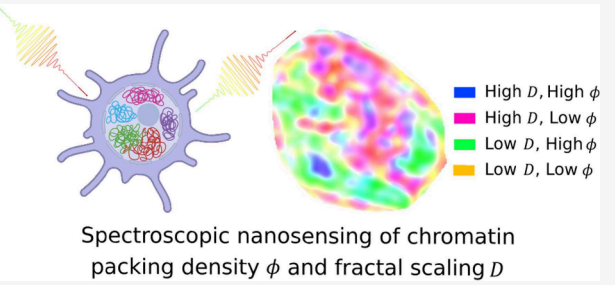

KEYWORDS: *spectroscopic nanosensing, chromatin imaging, finite difference time domain simulation*

INTRODUCTION

The human genome, nearly 2 m in length, is confined within a nucleus only a few microns in size. This extraordinary compaction is not arbitrary, following a highly organized hierarchical structure that facilitates essential biological functions, such as transcription, replication, and repair. At the nanoscale, chromatin—the complex of DNA and histone proteins—forms chromatin domains, discrete regions with specific packing properties. These domains, typically 50−200 nm in size, are characterized by their packing density (ϕ) and their fractal dimension (D). Fractal scaling behavior can be described mathematically as $M \propto r^D$, where M represents the total mass of chromatin within a domain, r is the domain radial length, and D quantifies how chromatin fills space within the domain topologically, ranging from $D = \frac{5}{3}$ for polymer self-avoiding random walk to $D = 3$ for maximal space filling.[1] Recent studies[2] have found chromatin domains exist across a continuous spectrum of structural states. At one extreme, low-density nascent domains emerge through processes such as loop extrusion and transcription-mediated contacts. At the other end, dense and stable domains form cores that support transcriptional machinery at their boundaries while maintaining structural integrity. Importantly, this model challenges the traditional binary classification of chromatin into "open" euchromatin and "closed" heterochromatin.[3,4] Instead, domains represent a dynamic, fractal-like system where the chromatin structure evolves in response to biochemical and physical cues. Moreover, on a larger length scale, domains converge into space-filling territories with various packing density ϕ, defined by the total space volume divided by the sum of domain volumes $\left(\frac{\sum V_{\text{domain}}}{V}\right)$. This structural organization underpins the regulation of transcriptional activity, with intermediate densities offering optimal conditions for transcription factor binding and RNA polymerase activity.[2]

Partial wave spectroscopic (PWS) microscopy is a label-free, live-cell, and high-throughput chromatin imaging modality using wide field visible light illumination.[5] As a diffraction-limited technique, PWS senses chromatin packing characteristics without resolving the actual subresolution packing structures. Instead, it utilizes the spectroscopic backscattering signal originating from the nanoscale spatial variations. In this paper, we exploit the capabilities of PWS by using the finite difference time domain (FDTD) method.[6]

Received: February 7, 2025
Revised: June 16, 2025
Accepted: June 30, 2025

RESULTS AND DISCUSSION

PWS Theory. The theory and instrumentation of PWS imaging has been described elsewhere.[7,8] Briefly, PWS is an interference-based label-free live-cell spectroscopic microscopy technique that senses the backscattering caused by heterogeneous alterations of packing structures $n_\Delta(\mathbf{r})$. Illuminated by a broadband visible LED, the backscattered light from $n_\Delta(\mathbf{r})$ interferes with the reference wave reflected from the glass-sample interface. This interference produces a spectrally resolved intensity signal $I(k)$, where k is the wavenumber. Overall, the collected wavenumber-dependent intensity has been described as[7]

$$I(x', y', k) = {\Gamma_{01}}^2 - 2\Gamma \,\mathrm{Im}\left\{\int_{-\infty}^{+\infty} k n_{1D}(\mathbf{r}) e^{-i2kz}\,\mathrm{d}z\right\} \tag{1}$$

where Γ_{01} is the Fresnel coefficient determined by the refractive index (RI) mismatch between the cell nucleus and the glass substrate, $\Gamma = \Gamma_{01}T_{01}T_{10}$ where T_{01} and T_{10} are Fresnel transmission coefficients of the same interface, Im means the imaginary part, $n_{1D}(\mathbf{r})$ is the RI variance $n_\Delta(\mathbf{r})$ convolved with the unitary Fourier transform of the microscope's pupil function T_{kNA} and a windowing function $T_{\mathbf{k}_s}$ within the direction of propagation k_s, $n_{1D}(\mathbf{r}) = \mathcal{F}_\perp\{T_{kNA}T_{\mathbf{k}_s}\} \otimes_\perp n_\Delta(\mathbf{r})$ specifically, and z is the propagation direction of the light wave. See ref 7 for details.

The two terms in this spectroscopic intensity signal can be used to extract ϕ and D, respectively. The first term in eq 1, ${\Gamma_{01}}^2$, is independent of k and is determined by the glass-nucleus RI mismatch. With the glass RI being a constant, ${\Gamma_{01}}^2$ carries the information on nucleus average RI. We estimate the nucleus RI $n_{nucleus}$ considering ϕ portion of the space is occupied by chromatin mass and the rest $(1-\phi)$ is occupied by water and mobile crowders, described through the Gladstone-Dale equation as[9,10]

$$n_{nucleus} \approx 1.345 + 0.089\phi \tag{2}$$

The second term in eq 1 is wavenumber dependent and reflects the chromatin packing scaling information. We have previously derived that the standard deviation of intensity across wavelengths, Σ^2, can be associated with packing scaling D. Briefly, the spectral variance quantifies the RI fluctuations' power spectral density (PSD) $\Phi_n(k)$

$$\Sigma^2 = \frac{R{k_c}^2 L}{\Delta k}\int_{T_{3D}} \mathbf{\Phi}_{\mathbf{n}_\Delta}(\mathbf{k})\,\mathrm{d}^3\mathbf{k} \tag{3}$$

where R is the Fresnel reflectance coefficient, k_c and Δk are incident central wavenumber and wavenumber range, respectively, L is sample thickness, T_{3D} is the frequency space coherence volume, a combination of T_{kNA} and limited illumination bandwidth $T_{\Delta\mathbf{k}_s}$.[7]

The association of optical measurements with material distribution, as described in eq 3, is achieved through the application of the Wiener-Khinchin theorem. This theorem is fundamental in that it defines the PSD $\mathbf{\Phi}_{\mathbf{n}_\Delta}(\mathbf{k})$ and autocorrelation functions (ACF) as Fourier-transform pairs. In the field of scattering, the Henyey-Greenstein phase function is often used to model material scattering characteristics. Here, we used a more robust and inclusive model, $B_\rho(r)$, a group of modified Whittle-Matérn mass-density ACF with shape parameter D_B to describe the randomness of chromatin packing, of which the Henyey-Greenstein model is a special case of $D_B = 3$.[10]

$$B_\rho(r) = A r^{D_B-3}\left[\Gamma\left(\frac{r}{l_{max}}, 3-D_B\right) - \Gamma\left(\frac{r}{l_{min}}, 3-D_B\right)\right] \tag{4}$$

where A is a normalization parameter, $\Gamma(x, a)$ is the upper incomplete gamma function, and l_{min} and l_{max} are lower and upper length scale of the power-law fractal regime, respectively. By taking the 3D Fourier transform of eq 4 and substituting into eq 3, we were able to correlate Σ^2 with D_B and then D_B to packing scaling D[10]

$$D = 3 + \left.\frac{\partial(\log B_\rho)}{\partial(\log r)}\right|_{r=r_0} \tag{5}$$

where r_0 is located within the $[l_{min}, l_{max}]$ range.

Overall, the theoretical framework described above lays out the framework for the measurement of multiplexed ϕ and D distribution for arbitrary materials with random RI fluctuations, using the hyperspectral PWS nanosensing platform, from the average and standard deviation of the spectra, respectively.

We first tested the accuracy of the framework when imaging large regions with uniform ACF distributions. We numerically created random material (2 μm in x, y, and z dimensions) that have varying mean RI (corresponding to varying effective ϕ according to eq 2, Figure 1a) or varying D_B (corresponding to varying effective D according to eq 5, Figure 1b), with 5 repetitions in each group. Simulated PWS signals $I_{FDTD}(x', y',$ and $k)$ were acquired and decomposed as in eq 1 and then averaged across the field of view.

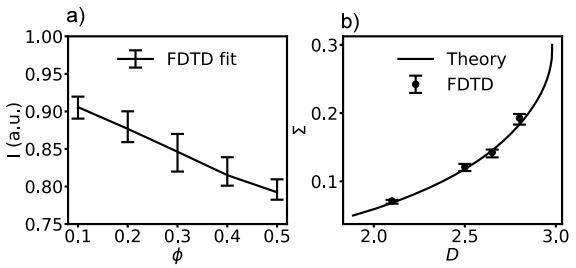

Figure 1. (a) FDTD simulation of average backscattering intensity (normalized by backscattering intensity of the glass-nucleus interface) as a function of effective nucleus ϕ. (b) Theoretical model and FDTD simulation of Σ to D conversion.

First, we try to establish a connection between average RI and Γ_{01}. For normal incident onto semi-infinite homogeneous media, ${\Gamma_{01}}^2$ can be expressed as $\left|\frac{n_{nucleus}-n_{glass}}{n_{nucleus}+n_{glass}}\right|^2$. For PWS microscopy with moderate incident numerical aperture (NA) and thin and heterogeneous media, a closed-form solution of Γ_{01} is tedious. Instead, we prepared five groups of random material with different effective ϕ values and calculated the average spectral intensity. Figure 1a shows that, with the increase in mean RI and thus effective ϕ, the RI miss-match between the media ($n < 1.45$) and glass ($n = 1.517$) decreases, leading to reduced normalized backscattering intensity as expected. This fitted $I-\phi$ curve is used as a lookup table to find the average RI of any material. Next, we test the accuracy of the "Σ-to-D conversion" model. The model itself establishes

https://doi.org/10.1021/acsphotonics.5c00311
ACS Photonics XXXX, XXX, XXX−XXX

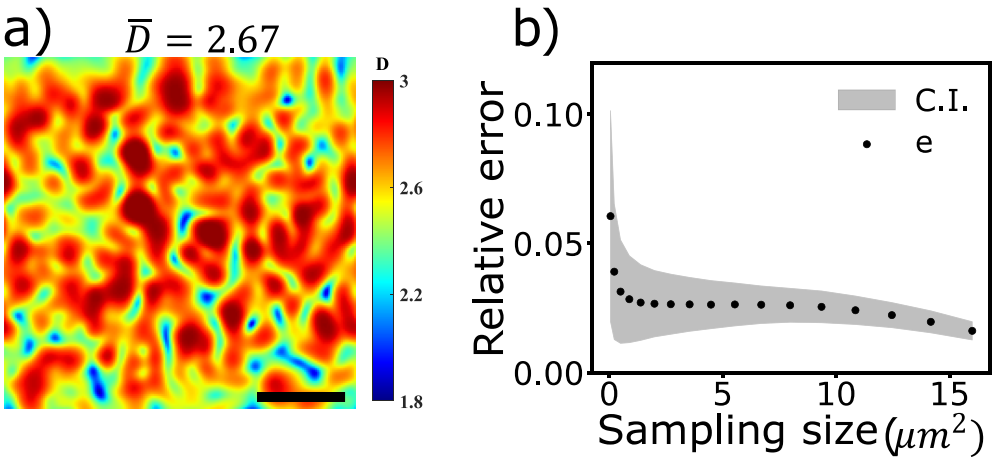

Figure 2. (a) FDTD synthesized PWS 2D D map for one random material with packing scaling D = 2.65. Scale bar: 1 μm. (b) Relative error "e" and confidence interval "C.I." of spatial average D as it relates to sampling size.

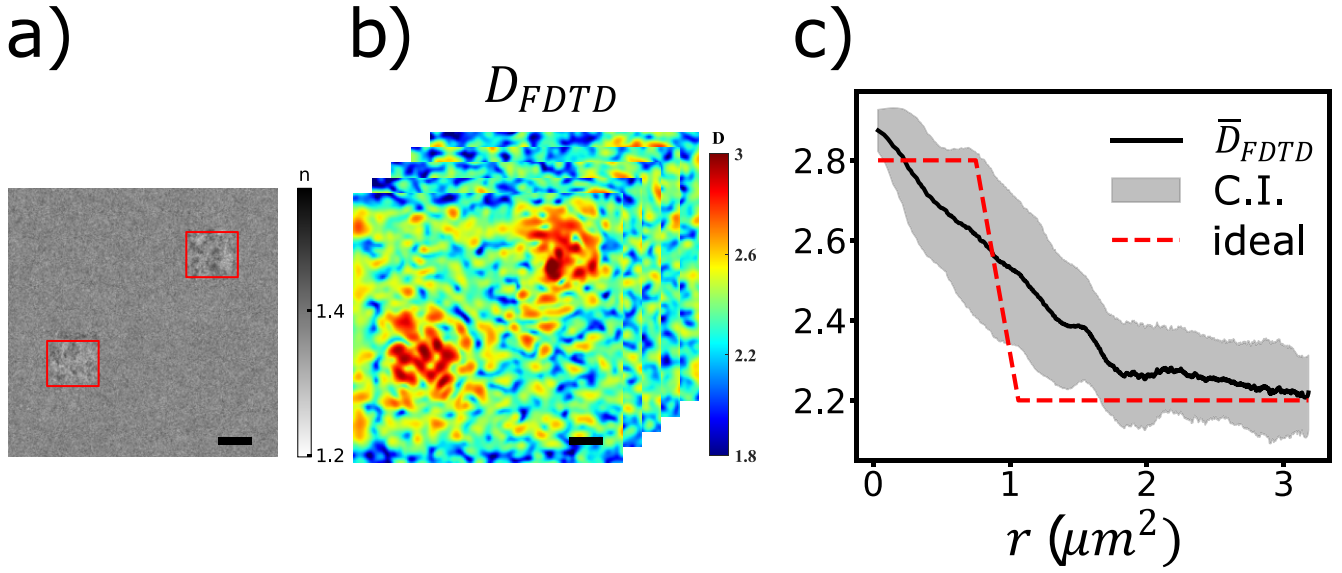

Figure 3. (a) XY cross section of RI distribution of random materials used for FDTD simulation, with high D region boundaries marked in red. (b) Corresponding simulated PWS D maps from FDTD. (c) Average D value and confidence interval (C.I.) as it relates to the distance from high D region centers. Scale bar: 1 μm for (a) and (b).

a monotonic $\Sigma - D$ curve under a given imaging setup. We then acquire the FDTD simulated PWS response of 4 groups of random material with different effective D values and evaluate their average spectral variance accordingly. Figure 1b illustrates the agreement between the theoretical model for Σ and simulated PWS results. These results demonstrate that the PWS sensed parameters match the material setup when averaging across a large region.

Effective Spatial Resolution. While PWS operates as a wide-field microscopy technique and is therefore diffraction-limited, this limitation does not hinder its utility. Unlike imaging techniques that rely on resolving spatial structures, the strength of PWS lies in its ability to derive ϕ and D from nanoscale RI fluctuations. These derived parameters provide statistical information about chromatin organization on scales well below the diffraction limit.

However, when a single PWS pixel displays values of D and ϕ, this value does not necessarily correspond to that pixel alone. This is because the scattering signal collected at any given pixel originates from an optical coherence volume, encompassing contributions from a spatially extended region centered at that pixel. The optical coherence volume is determined by the optics setup. PWS takes incident illumination from 500 to 700 nm, with a high collection NA (NA_c = 1.49) and a moderate incident NA (NA_i = 0.52). See Supporting Information about how these parameters are determined for the purpose of effectively measuring chromatin ultrastructure. With the fixed optical setup, we seek to quantify how large this effective spatial resolution region is and how it influences the interpretation of ϕ and D values across the field of view.

To quantify the spatial confidence of PWS-derived D measurements, we first simulated a uniform random medium to analyze how spatial averaging affects the measurement accuracy. We generated a random media (4 μm × 4 μm × 2 μm) following a single ACF with D = 2.65. Figure 2a shows the simulated FDTD D map, where the average D value closely matches the setup value, as expected. To evaluate the effect of spatial averaging, we sampled square-shaped zones with varying length Δx at random locations on the D map and

https://doi.org/10.1021/acsphotonics.5c00311
ACS Photonics XXXX, XXX, XXX−XXX

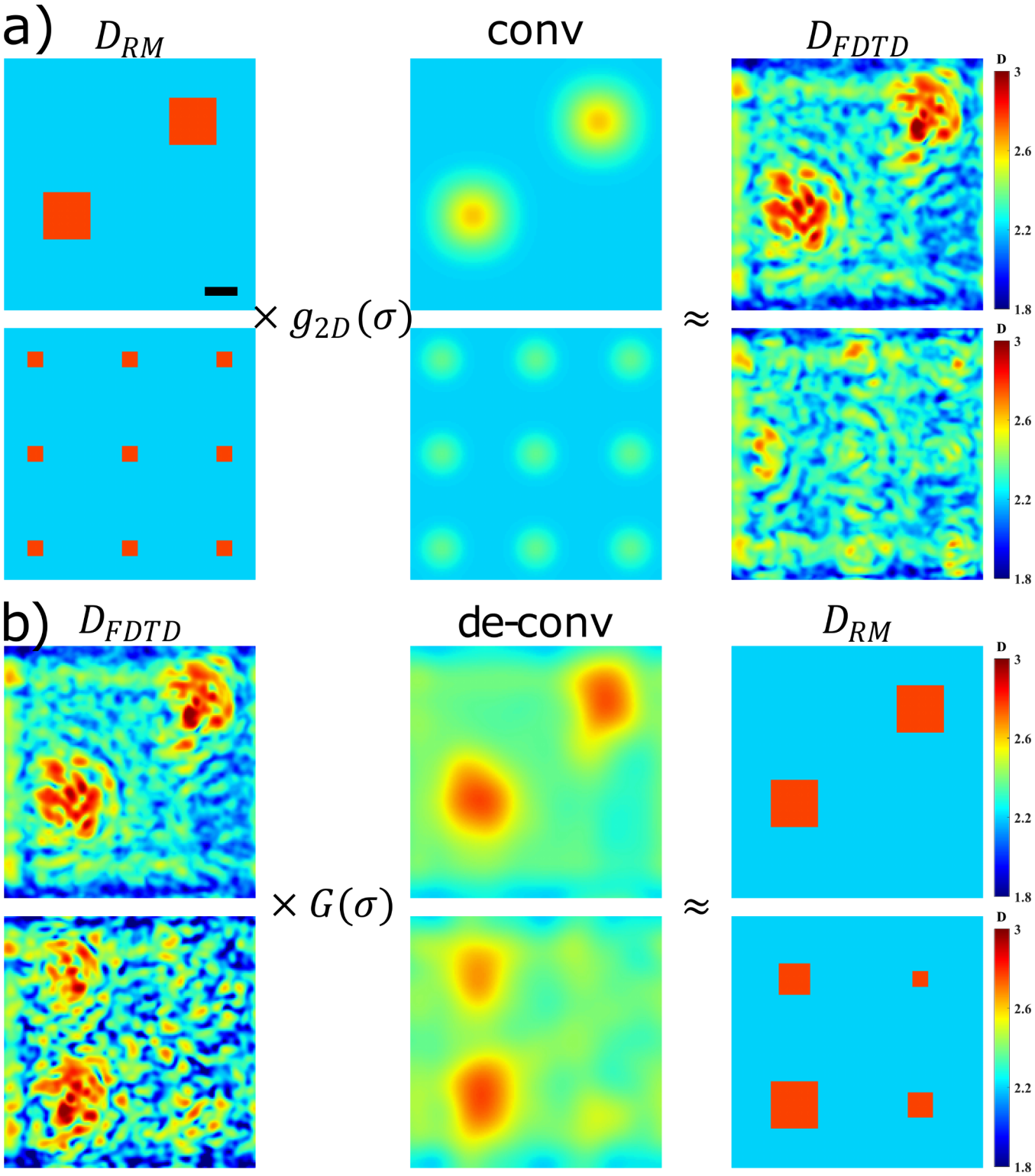

Figure 4. (a) PWS D measurement has an effective Gaussian filter. PWS D map (right) matches the material D distribution (left) convolved with a 2D Gaussian filter (middle) with σ = 0.49 μm. (b) Applying deconvolution on PWS D map (left) reconstructs material D distribution (middle) close to the input configuration (right). Scale bar: 1 μm.

calculated the relative error for each sampling size. As shown in Figure 2b, the measurement accuracy improves as the sampling size increases but plateaus at approximately 1.5 μm. This result highlights the effective spatial resolution limit of PWS, beyond which further averaging yields diminishing improvements in accuracy.

We have observed in experiments that the chromatin packing distribution within a cell nucleus is spatially heterogeneous with high-D regions of various shapes and sizes embedded within low-D regions. To mimic such characteristics, we created a simulation space containing two small high-D regions (1.5 μm × 1.5 μm × 2 μm, D = 2.8)

https://doi.org/10.1021/acsphotonics.5c00311
ACS Photonics XXXX, XXX, XXX−XXX

surrounded by a large low D background (8 μm × 8 μm × 2 μm, D = 2.2), as shown in Figure 3a. Five repetitions of such simulations are performed to minimize numerical uncertainties, as shown in Figure 3b.

Comparing the simulated PWS images to the material setup, we observed that the high-D regions appear larger in size but lower in value. This behavior is consistent with the effect of a spatial 2D Gaussian filter. The reasoning behind this observation, integration of scattering contribution from the optical coherence volume, was explained earlier.

Quantitatively, we measured the $D(r)$ distribution (average and confidence interval) starting from the centers of the two high-D regions and compared it to the ideal $\tilde{D}(r)$ measured from the material setup. As shown in Figure 3c, the effect of Gaussian blurring can be observed.

Since Gaussian blurring arises from averaging within the optical coherence volume, we hypothesize that the standard deviation σ of the Gaussian filter remains insensitive to the heterogeneity of the material RI randomness. To validate this hypothesis, we simulated PWS images of high D regions with various sizes (squares with length L_1 = 1.5 μm (Figure 4a, top), L_2 = 1.0 μm, L_3 = 0.75 μm (see Supporting Information) and L_4 = 0.5 μm (Figure 4a, bottom)) embedded in large (L = 8 μm) low D backgrounds.

For each simulation setup (shown in the left column of Figure 4a), we applied the same 2D Gaussian filter to the D_{RM} configurations. By minimizing the difference between the blurred D maps with different feature sizes (middle column) and the FDTD simulated PWS images (right column), we found the optimal σ of the Gaussian filter to be 0.49 ± 0.08 μm. The convergence of the σ value confirms that the spatial smoothing effect is insensitive to the structural feature sizes, and thus, deconvolution-based reconstruction is feasible.

With the optimal σ identified, we performed image deblurring by applying the Wiener filter algorithm to the simulated PWS images. For the four "high-D-regions-in-low-D-background" setups, the deconvolved images successfully recovered D distributions that closely match the original D maps, as shown in Figure 4b, top and Supporting Information. To further evaluate the algorithm's effectiveness under complex scenarios, we applied it to a simulation setup containing four high-D regions of varying sizes (L_1^2 to L_4^2) within a single field of view (Figure 4b, bottom). Visually, the reconstruction quality increases as the region size increases, L^2. Given that features larger than 1 μm^2 were effectively reconstructed, this finding confirms the utility of the deconvolution method for recovering packing information at the chromosome level.

Finally, we evaluated the ability of PWS to simultaneously decompose the information on ϕ and D while assessing its spatial resolution. To this end, we designed a simulation grid shown in Figure 5a consisting of 4 compartments having different combinations of ϕ and D. The top 2 compartments have low D (D = 2.1) while the bottom 2 compartments have high D (D = 2.65). Similarly, the left 2 compartments have high ϕ = 0.8 while the right have low ϕ = 0.2. Figure 5b,c shows the derived ϕ map and D map from the hyperspectral signal, respectively, demonstrating PWS's ability to distinguish the two properties. To further enhance the spatial resolution, the derived maps were processed with the deconvolution algorithm. The combined information is shown in Figure 5d, colored using the same scheme as in Figure 5a. As can be observed, the postprocessed PWS image is capable of acquiring

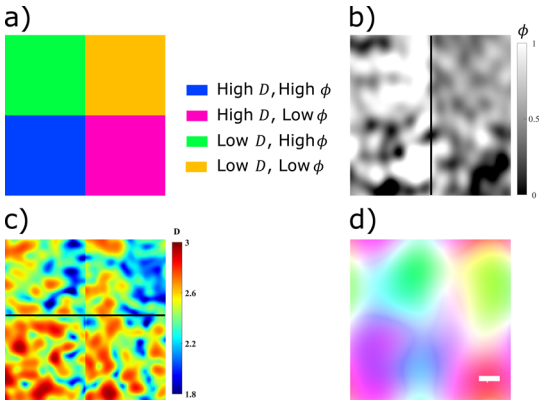

Figure 5. PWS is capable of measuring D and ϕ simultaneously. (a) Simulation grid setup with 4 regions, each with different D–ϕ combinations. (b) Simulated ϕ and (c) D map, with vertical or horizontal lines showing the expected separation. (d) Multiplexed view of the simulated PWS image with both D and ϕ information. Scale bar: 1 μm.

the ϕ and D information simultaneously, with clear boundaries between distinct regions consistent with the material configuration.

Experimental Validation. Experimentally, we use PWS to study chromatin ϕ and D. This is feasible for the following reasons. First, nucleus fills the PWS depth of imaging, becoming the major contributor of the scattering signal given proper cell culture (see Supporting Information for detail). Moreover, the Whittle-Matérn ACF has proven to be capable of modeling the chromatin mass density distribution given proper parameter choice.[10] Therefore, the optical sensed readouts can be converted to chromatin mass densities ϕ and D.

Resolving this nanoscale heterogeneity of chromatin is a complicated task, and there is an increasing number of imaging methods developed to probe different aspects of such information. At the smallest length scales, electron microscopy with specific DNA labeling has been developed,[11] achieving nanometer-level spatial resolution. While considered the ground truth measurement, chromTEM and chromSTEM are limited to imaging fixed cells and are both time-consuming and costly. Super resolution imaging modalities, like stochastic optical reconstruction microscopy (STORM), have allowed for direct measurement of spatial distribution of DNA, RNA, and proteins at sub 10 nm resolution.[12,13] However, STORM also requires fixed cells for imaging, precluding its use for live-cell studies. Additionally, STORM relies on fluorescent labels whose positions may not faithfully represent the true molecular locations due to the size and binding properties of the probes, introducing potential spatial inaccuracies.

There is also a variety of label-free optical phase-based or spectroscopic methods that aim to probe chromatin characteristics. Angle-resolved low-coherence interferometry (a/LCI) measures nuclear size and density at submicron level accuracy.[14] Quantitative phase imaging (QPI) techniques, such as spatial-light interference microscopy (SLIM) and digital holographic microscopy (DHM), yield high-contrast dry mass distribution across the nucleus.[15] Optical diffraction tomography (ODT) reconstructs full 3D RI tomograms with high fidelity.[16] Dynamic interferometric modalities, ChiSCAT's speckle-based motif discovery,[17] high-speed DYNAMICS imaging of chromatin fluctuations,[18] and dynamic full-field

https://doi.org/10.1021/acsphotonics.5c00311
ACS Photonics XXXX, XXX, XXX−XXX

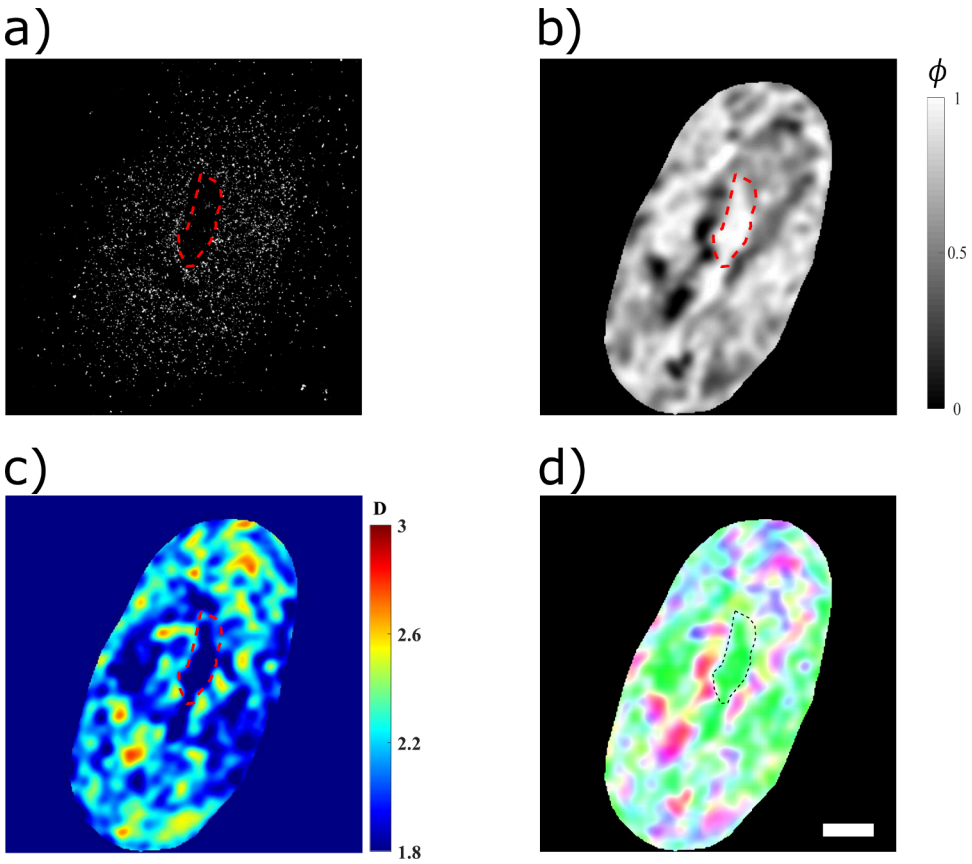

Figure 6. Experimental implementation of PWS deconvolution and $D-\phi$ multiplexing. (a) STORM image of RNAP II labels of a m248 ovarian cancer cell, with the manually drawn dashed line marking the nucleolus zone. (b) Corresponding PWS ϕ and (c) D measurement of the same nucleus. (d) Multiplexed PWS image of the same nucleus. Scale bar: 5 μm.

OCT (D-FFOCT)[19] of organelle motility, deliver unparalleled temporal and functional contrast. PWS uniquely bridges these gaps, enabling label-free, live-cell mapping of chromatin density ϕ and D in a single, high-throughput measurement. Below, we will be showing a few examples of using PWS alone or alongside other imaging modalities, gaining biological insights.

Figure 6 demonstrates the experimental utility of the above theoretical framework and analysis by comparing the imaging results between PWS and STORM. We labeled a m248 ovarian cancer cell using the RNA polymerase II (RNAP II) label and then imaged it with STORM (Figure 6a) and PWS (Figure 6b) simultaneously. At the center of Figure 6a, we identified one nucleolus based on the absence of RNAP II marks. We expect the nucleolus region to show a "low D, high ϕ" characteristic, as many proteins, rDNAs, and rRNAs support its function of ribosome biogenesis without chromatin-like ordered packing structures. Figure 6c shows the $D-\phi$ multiplexed image of the same nucleus acquired from a PWS system and analyzed following the method discussed earlier. Major parts of the nucleolus region are labeled green, which matches our expectation with some of its adjacent regions exhibiting different $D-\phi$ composition, suggesting distinct biological functions.

Next, we apply various epigenetic treatment on cell lines that induce chromatin morphological changes. As shown in Figure 7, we apply two different treatments, Actinomycin D (ActD) and $MgCl_2$, which induces a global decrease and increase in D, respectively. ActD intercalates preferentially at guanine–cytosine-rich regions of DNA, preventing strand separation and stalling RNA polymerase II. Since RNA polymerase II acts as a boundary element for packing domains, its removal disrupts local chromatin constraints. This leads to swelling, loss of domain organization, and the dissolution of packing domains, reflected by a decrease in the packing scaling D.[2,20,21] On the other hand, $MgCl_2$ increases the concentration of divalent cations, which neutralize electrostatic repulsion along the DNA backbone and promote chromatin condensation. In addition to charge neutralization, Mg^{2+} can form divalent cross-bridges between nucleosomes or DNA segments, further stabilizing the chromatin structure. These effects enhance the formation of nascent packing domains and stabilize existing mature domains, resulting in an increased number of packing domains and a higher packing scaling exponent D.[22,23] Figure 7a,c shows comparison of typical PWS D maps compared with their control group. Statistically, we collect the pixel-wise D values for all nuclei and compare the D distribution change. Figure 7b,d shows the D distribution change, revealing a statistically significant decrease for ActD treatment and an increase in $MgCl_2$, in good alignment with the theoretical predictions.

Moreover, we perform B-type lamin depletion, a treatment that majorly disturbs chromatin conformation at the periphery.[24] A large fraction of mammalian chromatin is tethered to the inner face of the nuclear envelope in so-called lamin-associated domains (LADs). With auxin-inducible degron of B-type lamins, we expect strong disruption of LADs and dissociation of genes from the nuclear periphery.

https://doi.org/10.1021/acsphotonics.5c00311
ACS Photonics XXXX, XXX, XXX−XXX

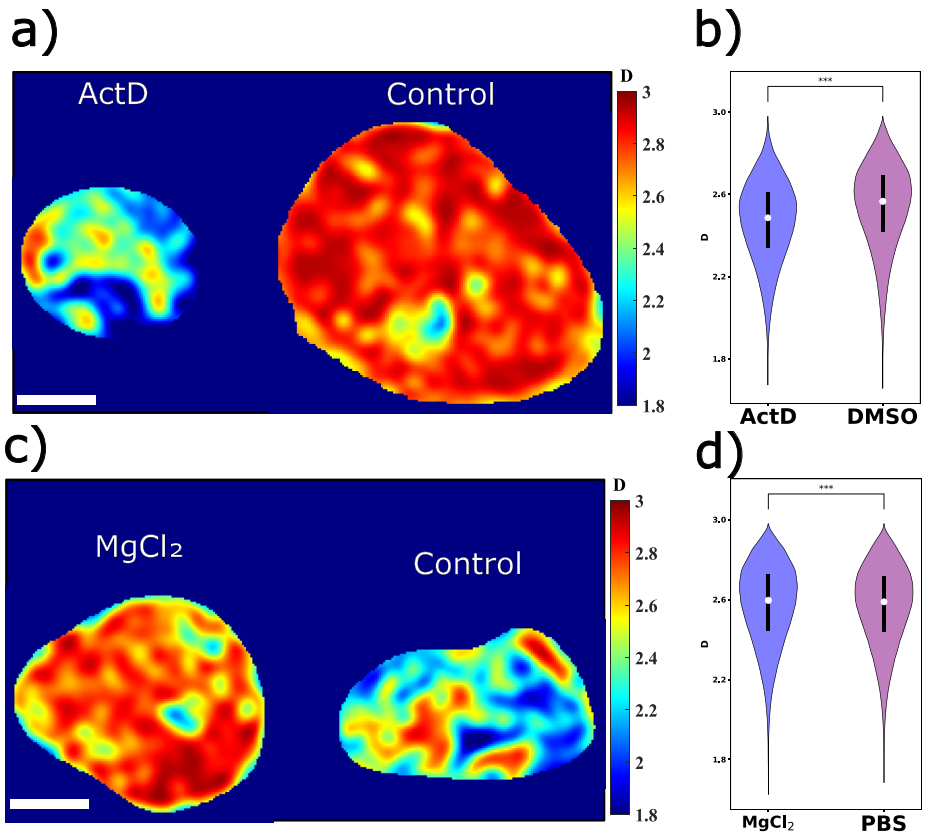

Figure 7. Typical experimental PWS image acquiring global change in D values with (a) ActD and (c) $MgCl_2$ treatment. Scale bars 5 μm. (b, d) D distribution comparison. ***$P < 0.001$.

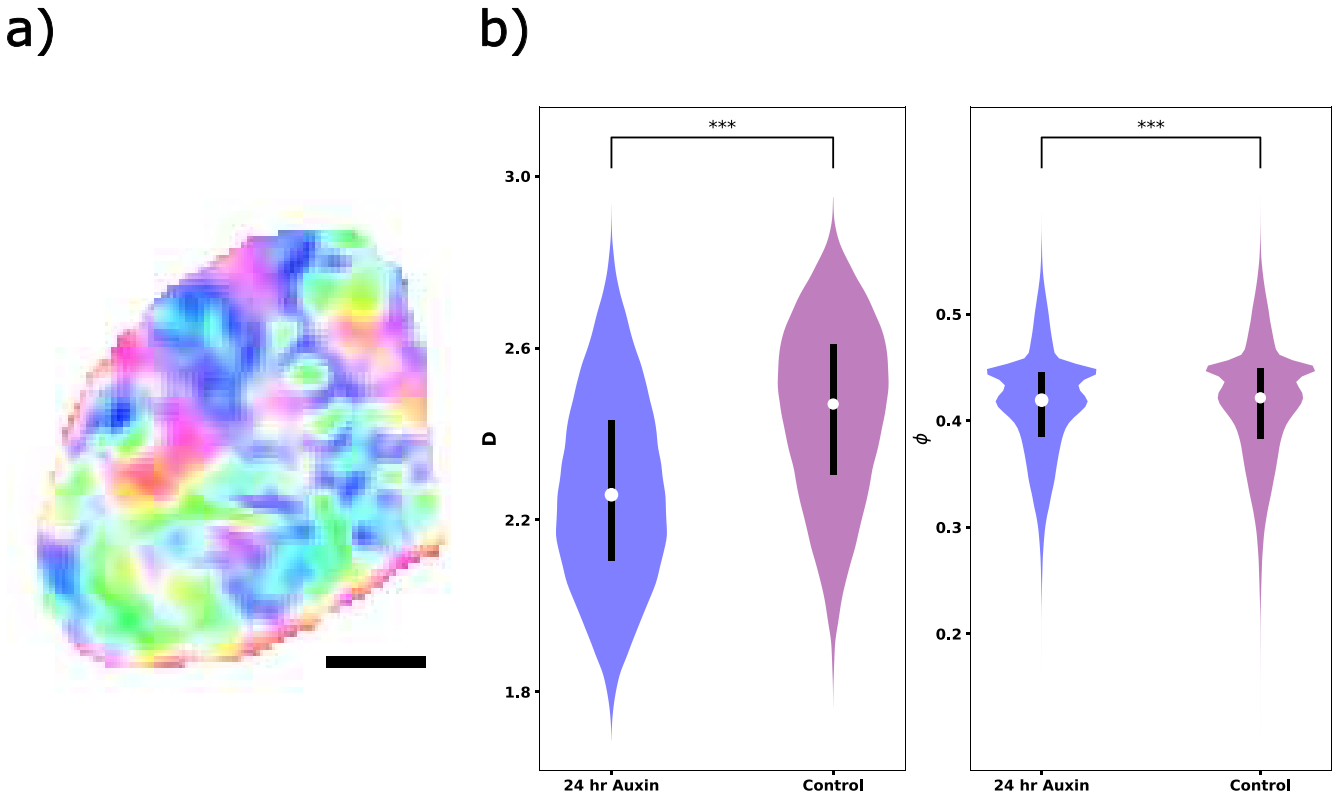

Figure 8. PWS analysis on B-type lamin depletion. (a) PWS $D-\phi$ multiplexed image of a typical untreated cell. Scale bar: 5 μm. (b) Nuclear periphery D and ϕ distribution comparison between 24 h Auxin treatment and control. ***$P < 0.001$.

https://doi.org/10.1021/acsphotonics.5c00311
ACS Photonics XXXX, XXX, XXX−XXX

We first look at a PWS $D-\phi$ multiplexed image of a typical untreated cell, shown in Figure 8a. The multiplexed image shows a high D distribution (blue and pink in color) at the nuclear exterior, where undistributed, heterochromatin-rich LADs are located. To test our hypothesis, we want to compare the D and ϕ distribution differences after treatment for pixels that are at the periphery. In order to do that, for each nucleus, we split it into 7 concentric layers whose shape mirrors the shape of the nucleus. D and ϕ values within the outmost ring are collected, as shown in Figure 8b. Statistically significant decreases in D and ϕ are observed after the lamin depletion treatment, in good agreement with the model.

CONCLUSION

In this paper, we explored the capacity of PWS microscopy to sense the chromatin ultrastructure, confirmed by FDTD-based simulations and experiments. By employing PWS, a label-free, high-throughput live-cell optical imaging modality, we were able to characterize the two important factors, D and ϕ, within a reasonable size confidence interval. We applied various epigenetic treatments that induce chromatin morphological changes, both globally and locally, and PWS microscopy is capable of capturing such changes. By combining PWS with other chromatin imaging modalities, this work opens up potential for better understanding of chromatin conformation, gene transcription, and better characterization of pathological conditions.

METHODS

Cell Culture. M248 cells were cultured in RPMI 1640 medium (Thermo Fisher Scientific, Waltham, MA; #11875127).

ActD treatment is performed on BJ fibroblasts cells (BJ CRL-2522), cultured in minimum essential media (no. 11095080, Thermo Fisher Scientific, Waltham, MA). ActD (#11805017, Gibco) is first dissolved in dimethyl sulfoxide (DMSO) and further diluted with cell media to make a working solution of 80 μM immediately before the experiment.

$MgCl_2$ treatment is performed on COV362 cells, cultured with Dulbecco's Modified Eagle Medium (DMEM) (Corning, Cat#10-017-CV), 10% FBS, 1% penicillin/streptomycin, and 1× GlutaMAX. $MgCl_2$ was purchased from Invitrogen (#AM9530G), and a 5 mM solution is used for treatment. Auxin treatment is performed on HCT116 cells. See ref 24 for a detailed experimental method.

STORM Imaging Buffer Preparations. A 1 M stock solution of DABCO [1,4-diazabicyclo-(2.2.2)-octane] (D27802, Sigma) was prepared by dissolution in distilled water with pH adjustment to 8.0 using 12 M HCl. The pH level is critical as it determines the final buffer's pH. The stock solution remains stable for several weeks when stored in dark conditions at 4 °C. Commercial DTT 1 M (43816, Sigma) was used as supplied and stored at 4 °C for several weeks. For sodium sulfite preparation (S0505, Sigma), a 1 M solution was made in 10× PBS and maintained at room temperature. Buffer preparation typically involved 40 mL batches, with pH adjustment using NaOH and HCl monitored by a pH meter, followed by refrigerated storage.

STORM Sample Preparation. The following primary antibody was stored at −20 °C after aliquoting goat antirat AF488 (ab252855) and was maintained at 4 °C. Cells were seeded in eight-well Lab-Tek Chambered cover glass (No. 1 borosilicate bottom) at 12.5k cells per well. Following a 48-h incubation, cells underwent fixation using 3% paraformaldehyde and 0.1% glutaraldehyde in PBS for 10 min. Subsequent steps included PBS washing, quenching with fresh 0.1% sodium borohydride in PBS (7 min), and triple PBS rinses at ambient temperature. Cell permeabilization was achieved using blocking buffer (3% BSA, 0.5% Triton X-100 in PBS) for 20 min. Primary antibody incubation utilized rabbit anti-RNAPII (Abcam) in blocking buffer for a minimum 2 h period at room temperature, followed by triple washes with washing buffer (0.2% BSA, 0.1% Triton X-100 in PBS). Secondary antibody labeling employed goat antirabbit AF647 (Thermo Fisher A21245) for 40 min, followed by three PBS washes at room temperature. Samples were stored at 4 °C after completing this initial target staining.

STORM System Configuration, Imaging, and PWS Coregistration. The STORM imaging system was constructed around a Nikon Eclipse Ti-E inverted microscope equipped with a perfect focus system. Illumination was provided by two laser systems: a multiwavelength OBIS Laser Box (Coherent) delivering 405, 488, 532, 552, and 637 nm emissions, complemented by a dedicated 532 nm green laser (MGL-FN-532, Changchun New Industries Optoelectronics Tech. Co., Ltd.). Laser output was collimated to deliver 3−10 kW/cm^3 at the sample plane. Image acquisition employed a Nikon SR APO TIRF 100× objective (1.49 NA) coupled to an Andor iXon Ultra 888 electron-multiplying CCD camera. Each wavelength channel captured a minimum of 10,000 frames at 30 ms exposure intervals. Total Internal Reflectance Fluorescence (TIRF) illumination generated an evanescent wave penetrating approximately 200 nm from the glass-cell interface, with the focal plane adjustment optimized for fluorophore excitation. The imaging of RNA Polymerase II (AF488) utilized a 488 nm laser. Partial Wave Spectroscopic (PWS) measurements utilized low numerical aperture illumination (NA_i = 0.52), with image collection performed through a 100× objective. The optical path incorporated a liquid crystal tunable filter (LCTF; CRI VariSpec) positioned before an sCMOS detector (ORCA Flash 4.0, Hamamatsu). Spectral resolution was achieved through the LCTF, enabling wavelength-resolved image acquisition across the 500−700 nm range at 2 nm increments. Image coregistration between PWS and STORM data sets was accomplished through the acquisition of reference brightfield and fluorescence images on both camera systems. These reference images were used to generate a homograph-based transformation matrix, which was subsequently applied to the PWS image. The region of interest (ROI) defined for the STORM acquisition was then mapped onto the transformed PWS image.

FDTD Simulation. Throughout this study, we used Angora,[25] a "microscope-in-a-computer" simulation software implementing the FDTD method, as a consistent testing method. Light-matter interaction was simulated via the FDTD method following experimental PWS setup, and the back-scattering signal was collected to generate simulation PWS images. The simulation spaces are created with a rectangular Cartesian FDTD grid with $\Delta x = \Delta y = \Delta z = 15$ nm. Courant factor $\left(\sqrt{3}\frac{c\Delta t}{\Delta x}\right)$ is set to 0.98.

The main simulation space consists of two layers. A layer of uniform material (n = 1.517, h = 1 μm) is used to represent the glass holder substrate. On top of that are numerically created 3D random media with varying sizes and RI distributions.

https://doi.org/10.1021/acsphotonics.5c00311
ACS Photonics XXXX, XXX, XXX−XXX

Briefly, one first decides the x, y, z size of the material and creates an empty grid following the FDTD grid size. Next, one must choose proper parameters of the ACF as discussed in eq 4. The 1D ACF is expanded into 3D, as it is the same size of the material grid. Then, the material grid is filled with zero-mean random values whose ACF follows the 3D ACF. Next, the 3D material value is shifted up to the designated average RI value, finishing the construction of 3D random material that has desired D and ϕ. Perfectly-Matched Layers (PMLs) of 5 grid thick surround the simulation space to reduce artificial reflection at space boundaries.

In the time domain, a sinusoidally modulated Gaussian time waveform is used to represent the 500−700 nm wide spectrum incident. A collection of plane waves with different incident angles, θ, and polarizations, ψ, are used to mimic the experimental incident and collection NA. A near-field-to-far-field transformer (NFFFT) is used to synthesize far-field images from the simulation collected near-field electromagnetic waves.

The Angora software utilizes parallel CPU computing to reduce the time needed for each simulation.

■ ASSOCIATED CONTENT

Data Availability Statement

The data underlying this study are openly available at https://github.com/BackmanLab/RM-FDTD-PWS. Angora is a free, open-source software available at https://github.com/BackmanLab/AngoraFDTD.

Supporting Information

The Supporting Information is available free of charge at https://pubs.acs.org/doi/10.1021/acsphotonics.5c00311.

> The convolution and deconvolution reconstruction quality for all high-D region sizes; the coloring scheme for $D - \phi$ multiplexing; optimization of optical parameters; discussion on imaging depth (PDF)

■ AUTHOR INFORMATION

Corresponding Authors

Geng Wang − *Center for Physical Genomics and Engineering and Department of Biomedical Engineering, Northwestern University, Evanston, Illinois 60208, United States;* orcid.org/0000-0002-5615-4696; Email: wanggeng@northwestern.edu

Vadim Backman − *Center for Physical Genomics and Engineering and Department of Biomedical Engineering, Northwestern University, Evanston, Illinois 60208, United States;* orcid.org/0000-0003-1981-1818; Email: v-backman@northwestern.edu

Authors

Yuanzhe Su − *Center for Physical Genomics and Engineering and Department of Biomedical Engineering, Northwestern University, Evanston, Illinois 60208, United States;* orcid.org/0000-0003-1110-2822

Luay M. Almassalha − *Department of Biomedical Engineering, Northwestern University, Evanston, Illinois 60208, United States; Department of Gastroenterology and Hepatology, Northwestern Memorial Hospital, Chicago, Illinois 60611, United States*

Nicolas Acosta − *Center for Physical Genomics and Engineering and Department of Biomedical Engineering, Northwestern University, Evanston, Illinois 60208, United States*

Cody L. Dunton − *Center for Physical Genomics and Engineering and Department of Biomedical Engineering, Northwestern University, Evanston, Illinois 60208, United States*

Karla I. Medina − *Center for Physical Genomics and Engineering and Interdisciplinary Biological Sciences Graduate Program, Northwestern University, Evanston, Illinois 60208, United States*

Emily Pujadas Liwag − *Center for Physical Genomics and Engineering and Interdisciplinary Biological Sciences Graduate Program, Northwestern University, Evanston, Illinois 60208, United States*

Complete contact information is available at: https://pubs.acs.org/10.1021/acsphotonics.5c00311

Funding

National Institutes of Health (NIH) grants R01CA225002, R01CA228272, T32AI083216, T32GM142604, U54CA261694, and U54CA268084. National Science Foundation (NSF) grants EFMA-1830961, CBET-2430743, and CBET-2427519.

Notes

The authors declare no competing financial interest.

■ ACKNOWLEDGMENTS

Computational resources of this research were supported in part through the computational resources and staff contributions provided for the Quest high performance computing facility at Northwestern University, which is jointly supported by the Office of the Provost, the Office for Research, and Northwestern University Information Technology. The authors thank Prof. Igal Szleifer, Dr. Rikkert J. Nap, Dr. Marcelo A. Carignano, and Paola Carillo Gonzalez for helpful discussions. The authors thank Benjamin Keane for proof reading.

■ REFERENCES

(1) Virk, R. K. A.; Wu, W.; Almassalha, L. M.; Bauer, G. M.; Li, Y.; VanDerway, D.; Frederick, J.; Zhang, D.; Eshein, A.; Roy, H. K.; Szleifer, I.; Backman, V. Disordered chromatin packing regulates phenotypic plasticity. *Science Advances* **2020**, *6*, eaax6232.

(2) Almassalha, L. M. Chromatin conformation, gene transcription, and nucleosome remodeling as an emergent system. *Science Advances* **2025**, *11*, eadq6652.

(3) Dekker, J.; Mirny, L. A. The chromosome folding problem and how cells solve it. *Cell* **2024**, *187*, 6424−6450.

(4) Carignano, M. A.; Kroeger, M.; Almassalha, L. M.; Agrawal, V.; Li, W. S.; Pujadas-Liwag, E. M.; Nap, R. J.; Backman, V.; Szleifer, I. Local volume concentration, packing domains, and scaling properties of chromatin. *eLife* **2024**, *13*, RP97604.

(5) Almassalha, L. M.; Bauer, G. M.; Chandler, J. E.; Gladstein, S.; Cherkezyan, L.; Stypula-Cyrus, Y.; Weinberg, S.; Zhang, D.; Thusgaard Ruhoff, P.; Roy, H. K.; Subramanian, H.; Chandel, N. S.; Szleifer, I.; Backman, V. Label-free imaging of the native, living cellular nanoarchitecture using partial-wave spectroscopic microscopy. *Proc. Natl. Acad. Sci. U. S. A.* **2016**, *113*, E6372−E6381.

(6) Teixeira, F. L.; Sarris, C.; Zhang, Y.; Na, D.-Y.; Berenger, J.-P.; Su, Y.; Okoniewski, M.; Chew, W. C.; Backman, V.; Simpson, J. J. Finite-difference time-domain methods. *Nat. Rev. Methods Primers* **2023**, *3*, 1−19.

(7) Cherkezyan, L.; Capoglu, I.; Subramanian, H.; Rogers, J. D.; Damania, D.; Taflove, A.; Backman, V. Interferometric Spectroscopy

of Scattered Light Can Quantify the Statistics of Subdiffractional Refractive-Index Fluctuations. *Phys. Rev. Lett.* **2013**, *111*, 033903.
(8) Cherkezyan, L.; Zhang, D.; Subramanian, H.; Capoglu, I.; Taflove, A.; Backman, V. Review of interferometric spectroscopy of scattered light for the quantification of subdiffractional structure of biomaterials. *JBO* **2017**, *22*, 030901.
(9) Gladstone, J. H.; Dale, T. P. XIV. Researches on the refraction, dispersion, and sensitiveness of liquids. *Philosophical Transactions of the Royal Society of London* **1997**, *153*, 317−343.
(10) Eid, A.; Eshein, A.; Li, Y.; Virk, R.; Van Derway, D.; Zhang, D.; Taflove, A.; Backman, V. Characterizing chromatin packing scaling in whole nuclei using interferometric microscopy. *Opt. Lett., OL* **2020**, *45*, 4810−4813.
(11) Ou, H. D.; Phan, S.; Deerinck, T. J.; Thor, A.; Ellisman, M. H.; O'Shea, C. C. ChromEMT: Visualizing 3D chromatin structure and compaction in interphase and mitotic cells. *Science* **2017**, *357*, No. eaag0025.
(12) Schnitzbauer, J.; Strauss, M. T.; Schlichthaerle, T.; Schueder, F.; Jungmann, R. Super-resolution microscopy with DNA-PAINT. *Nat. Protoc* **2017**, *12*, 1198−1228.
(13) Bintu, B.; Mateo, L. J.; Su, J.-H.; Sinnott-Armstrong, N. A.; Parker, M.; Kinrot, S.; Yamaya, K.; Boettiger, A. N.; Zhuang, X. Super-resolution chromatin tracing reveals domains and cooperative interactions in single cells. *Science* **2018**, *362*, eaau1783.
(14) Zhu, Y.; Terry, N. G; Wax, A. Angle-resolved low-coherence interferometry: an optical biopsy technique for clinical detection of dysplasia in Barrett's esophagus. *Expert Review of Gastroenterology & Hepatology* **2012**, *6*, 37−41.
(15) Nguyen, T. L.; Pradeep, S.; Judson-Torres, R. L.; Reed, J.; Teitell, M. A.; Zangle, T. A. Quantitative Phase Imaging: Recent Advances and Expanding Potential in Biomedicine. *ACS Nano* **2022**, *16*, 11516−11544.
(16) Lee, D.; Lee, M.; Kwak, H.; Kim, Y. S.; Shim, J.; Jung, J. H.; Park, W.-s.; Park, J.-H.; Lee, S.; Park, Y. High-fidelity optical diffraction tomography of live organisms using iodixanol refractive index matching. *Biomed. Opt. Express, BOE* **2022**, *13*, 6404−6415.
(17) Trelin, A.; Kussauer, S.; Weinbrenner, P.; Clasen, A.; David, R.; Rimmbach, C.; Reinhard, F. ChiSCAT: Unsupervised Learning of Recurrent Cellular Micromotion Patterns from a Chaotic Speckle Pattern. *Nano Lett.* **2024**, *24*, 12374−12381.
(18) Hsiao, Y.-T.; Tsai, C.-N.; Chen, T.-H.; Hsieh, C.-L. Label-Free Dynamic Imaging of Chromatin in Live Cell Nuclei by High-Speed Scattering-Based Interference Microscopy. *ACS Nano* **2022**, *16*, 2774−2788.
(19) Scholler, J.; Groux, K.; Goureau, O.; Sahel, J.-A.; Fink, M.; Reichman, S.; Boccara, C.; Grieve, K. Dynamic full-field optical coherence tomography: 3D live-imaging of retinal organoids. *Light Sci. Appl.* **2020**, *9*, 140.
(20) Li, Y. Nanoscale chromatin imaging and analysis platform bridges 4D chromatin organization with molecular function. *Science Advances* **2021**, *7*, eabe4310.
(21) Kant, A.; Guo, Z.; Vinayak, V.; Neguembor, M. V.; Li, W. S.; Agrawal, V.; Pujadas, E.; Almassalha, L.; Backman, V.; Lakadamyali, M.; Cosma, M. P.; Shenoy, V. B. Active transcription and epigenetic reactions synergistically regulate meso-scale genomic organization. *Nat. Commun.* **2024**, *15*, 4338.
(22) Wang, Y.; et al. Chromatin Organization Governs Transcriptional Response and Plasticity of Cancer Stem Cells. *Advanced Science* **2025**, *12*, 2407426.
(23) Nap, R. J.; Carillo Gonzalez, P.; Coraor, A. E.; Virk, R. K. A.; de Pablo, J. J.; Backman, V.; Szleifer, I. The impact of charge regulation and ionic intranuclear environment on the nucleosome core particle. *J. Chem. Phys.* **2024**, *161*, 235101.
(24) Pujadas Liwag, E. M.; et al. Depletion of lamins B1 and B2 promotes chromatin mobility and induces differential gene expression by a mesoscale-motion-dependent mechanism. *Genome Biology* **2024**, *25*, 77.
(25) Çapoğlu, I. R.; Taflove, A.; Backman, V. Angora: A Free Software Package for Finite-Difference Time-Domain Electromagnetic Simulation. *IEEE Antennas and Propagation Magazine* **2013**, *55*, 80−93.

https://doi.org/10.1021/acsphotonics.5c00311
ACS Photonics XXXX, XXX, XXX−XXX